Energy & Environmental Science

PAPER

Seed-assisted synthesis of highly ordered TiO$_2$@α-Fe$_2$O$_3$ core/shell arrays on carbon textiles for lithium-ion battery applications†

Yongsong Luo,[abg] Jingshan Luo,[a] Jian Jiang,[a] Weiwei Zhou,[a] Huanping Yang,[a] Xiaoying Qi,[c] Hua Zhang,[c] Hong Jin Fan,[ab] Denis Y. W. Yu,[b] Chang Ming Li[de] and Ting Yu*[abf]

Highly ordered TiO$_2$@α-Fe$_2$O$_3$ core/shell arrays on carbon textiles (TFAs) have been fabricated by a stepwise, seed-assisted, hydrothermal approach and further investigated as the anode materials for Li-ion batteries (LIBs). This composite TFA anode exhibits superior high-rate capability and outstanding cycling performance. The specific capacity of the TFAs is much higher than that of pristine carbon textiles (CTs) and TiO$_2$ nanorod arrays on carbon textiles (TRAs), indicating a positive synergistic effect of the material and structural hybridization on the enhancement of the electrochemical properties. This composite nanostructure not only provides large interfacial area for lithium insertion/ extraction but should also be beneficial in reducing the diffusion pathways for electronic and ionic transport, leading to the improved capacity retention on cycling even at high discharge–charge rates. It is worth emphasizing that the CT substrates also present many potential virtues for LIBs as flexible electronic devices owing to the stretchable, lightweight and biodegradable properties. The fabrication strategy presented here is facile, cost-effective, and scalable, which opens new avenues for the design of optimal composite electrode materials for high performance LIBs.

[a] Division of Physics and Applied Physics, School of Physical and Mathematical Sciences, Nanyang Technological University, 637371, Singapore. E-mail: yuting@ntu.edu.sg
[b] Energy Research Institute at Nanyang Technological University (ERIAN), 639789, Singapore
[c] School of Materials Science and Engineering, Nanyang Technological University, 639798, Singapore
[d] Institute for Clean Energy and Advanced Materials, Southwest University, Chongqing 400700, P. R. China
[e] Division of Bioengineering, School of Chemical and Biomedical Engineering, Nanyang Technological University, 637371, Singapore
[f] Department of Physics, Faculty of Science, National University of Singapore, 117542, Singapore
[g] School of Physics and Electronic Engineering, Xinyang Normal University, Xinyang 464000, P. R. China
† Electronic supplementary information (ESI) available. See DOI: 10.1039/c2ee03396h

1. Introduction

In recent years, more urgent efforts have been advocated to combat global warming and to build green, environmentally friendly economies. Accordingly, scientists worldwide are searching for renewable energy sources to replace traditional fossil fuels and ease the crises resulting from environmental deterioration due to massive CO$_2$ emission. However, exploitation of alternative and green energy sources (solar, wind, tide, …) requires the efficient support of energy storage/conversion devices that can compensate their intermittent characteristics. In general, the energy storage systems for renewable sources must have properties optimized such as high energy density, high power density, good safety, long cycle life, use of low-cost

Broader context

Currently, rechargeable lithium-ion batteries (LIBs) have been considered as the most successful and prospective technologies that can repeatedly generate clean electricity from stored materials and convert reversibly electric energy into chemical energy, one of the most popular topics is the development of anode materials which play an important role in the determination of energy density, safety and life cycle of LIBs. In this contribution, we report on the preparation and electrochemical performances of highly ordered TiO$_2$@α-Fe$_2$O$_3$ core/shell arrays on carbon textiles (TFAs) for LIB applications. This configuration not only provides large interfacial area for fast lithium insertion/extraction but also reduces diffusion pathways for electronic and ionic transport. As a result, this assembly of TFAs exhibits a positive synergistic effect and displays superior electrochemical performances in terms of high rate capability, large reversible capacity and excellent cycle performance, holding great potential as a high-rate anode material for lithium storage.

This journal is © The Royal Society of Chemistry 2012

Energy Environ. Sci., 2012, **5**, 6559–6566 | 6559

abundant raw materials and cost-effective synthesis. Currently, rechargeable lithium-ion batteries (LIBs) have been considered as the most successful and prospective technologies that can repeatedly generate clean electricity from stored materials and convert reversibly electric energy into chemical energy.[1–4]

Conventional LIBs have become a key component of portable electronic devices due to their unique features such as high energy density, flexible lightweight design and a longer cycle life than other battery systems as listed above. In this regard, tremendous research efforts have been devoted to investigating the electrochemical performances of a wide variety of active materials and electrolytes in recent years.[5–8] Among these studies, one of the most popular topics is the development of anode materials which play an important role in the determination of energy density, safety and life cycle of LIBs.[9,10] Up to now, the anode materials have been mainly classified into three categories and investigated intensively, *i.e.*, carbonaceous materials, lithium alloys and transition metal oxides. Carbonaceous materials are the most used commercial anode materials for LIBs because of their several advantages: low cost, high abundance, favorable stability, and outstanding kinetics.[11,12] However, for this type of anode materials, the operating voltage is usually below 0.2 V *versus* Li/Li^{+} and very close to the lithium electroplating potential, especially at high rates, which would cause serious safety issues.[13–15] Lithium alloys are made up of some main-group elements (*e.g.*, Si, Ge, Sn, *etc.*) with lithium at a low potential.[16,17] Unfortunately, huge volume changes occur during the electrochemical lithiation/delithiation process.[18,19] Transition-metal oxides (M_xO_y, M = Fe, Co, Ni, *etc.*) can offer significantly higher electrochemical capacities than those of carbonaceous anodes.[20] Whereas similar to the Li-alloying process, the conversion reaction leads to severe volume variation that causes mechanical degradation, resulting in a rapid capacity loss especially at high charge–discharge rates. Further, the low conductivity of transition metal oxides often hastens the degradation process.[21–23] Many previous works have focused on adopting metal substrates as current collectors, mainly copper and aluminium, which were integrated with battery electrode materials through a directly growing or coating process. These substrates, therefore, present themselves to be more or less stiff or rigid rather than being flexible, lightweight, and environmentally friendly devices.[24,25]

To resolve the above-mentioned drawbacks, various metal oxides and carbonaceous materials with different geometrical attributes, morphological forms, and micro-architectures have been employed as anode materials for LIBs.[26–28] However, to the best of our knowledge, an anode combining hybrid metal oxide core/shell arrays with carbon textiles (CTs) for LIBs has not been reported. Herein, we report on the preparation and electrochemical performances of highly ordered $TiO_2@\alpha$-Fe_2O_3 core/shell arrays on carbon textiles (TFAs) for LIB applications. First, both the core and shell materials are abundant, low cost, and environmentally benign materials.[29,30] Moreover, titania has become an anode material for lithium storage since it exhibits a relatively high lithium insertion/extraction voltage at about 1.7 V.[31,32] This feature can efficiently avoid the formation of solid electrolyte interphase (SEI) layers and electroplating of lithium during the cycling process. Second, CT substrates offer many advantages for flexible electronic devices. In addition to being widely available and inexpensive, CTs are stretchable,

lightweight, biodegradable, and can be rolled or folded into three-dimensional (3D) configurations as well.[33–35] Moreover, the carbonaceous matrices can, to a large extent, prevent deterioration, preserve the integrity, and thus avoid the failure of the electrodes upon consecutive Li-ion insertion/extraction cycles.[4,36–38] Third, highly ordered active nanostructure arrays grown directly on current collectors have shown significant improvements in LIBs performance due to the remarkable advantages of this system such as good contact of the active materials and adhesion with the current collector as well as good strain accommodation.[39] This configuration not only provides large interfacial area for fast lithium insertion/extraction but also reduces diffusion pathways for electronic and ionic transport. Therefore, the durability, rate capability and undesirable side reactions are significantly improved. As a result, this assembly of the TFAs exhibits a positive synergistic effect and displays superior electrochemical performances in terms of high rate capability, large reversible capacity and excellent cycle performance, holding great potential as a high-rate anode material for lithium storage.

2. Experimental

Synthesis of TiO_2 nanorod arrays on carbon textiles (TRAs)

The TRAs were synthesized by a hydrothermal growth method.[40] In a typical process: the CTs substrate (1.5 × 4.0 cm) was first cleaned with deionized water, dried in air, and then coated with TiO_2 nanoparticles as seeds by an atomic layer deposition (ALD) technique.[41] Second, the precursor was prepared by adding 0.45 ml titanium butoxide to a well-mixed solution containing 15 ml of HCl and 15 ml of H_2O, this solution was stirred until the solution became clear. Third, the precursor was poured into a Teflon-lined stainless steel autoclave with the TiO_2 seed-assisted CTs substrate. The hydrothermal growth was conducted at 150 °C for 12 h in an electric oven.

Assembly of $TiO_2@\alpha$-Fe_2O_3 core/shell arrays on carbon textiles

The fabrication process of the TFAs was as follows: first, ZnO nanoparticles (50 nm thick) were deposited on the TRAs wall as sacrificial template.[39] Subsequently, the samples of ZnO-coated TRAs (Z-TRAs) were immersed in an aqueous solution of $Fe(NO_3)_3 \cdot 9H_2O$ (0.013 M) at room temperature for 24 h, ensuring the sufficient dissolution of ZnO nanoparticles. In this solution, $Fe(NO_3)_3 \cdot 9H_2O$ hydrolyzed to $Fe(OH)_3$ colloid on the surface of the TRAs while ZnO dissolved simultaneously in the solution with acids produced by $Fe(NO_3)_3 \cdot 9H_2O$ hydrolysis ($Fe^{3+} + 3H_2O \leftrightarrow Fe(OH)_3 + 3H^+$). After the immersion, the product was rinsed with distilled water, dried in environmental temperature, and treated at 450 °C in Ar for 5 h to obtain TFAs.

Characterization

The phase purity of the products was characterized by X-ray powder diffraction (XRD) using an X-ray diffractometer with Cu Kα radiation ($\lambda = 1.5418$ Å). Scanning electron microscopy (SEM) images and energy dispersive X-ray spectroscopy (EDS) analyses were obtained using a HITACHI S-4300 microscope (Japan). Transmission electron microscopy (TEM) and

high-resolution TEM (HRTEM) observations were carried out on a JEOL JEM-2010 instrument in bright field and on a HRTEM JEM-2010FEF instrument (operated at 200 kV). X-Ray photoelectron spectroscopy (XPS) spectra were measured on a Perkin-Elmer model PHI 5600 XPS system with a resolution of 0.3–0.5 eV from a monochromated aluminium anode X-ray source. The surface area was measured using a Micromeritics (NOVA 4200e) analyzer. The nitrogen adsorption and desorption isotherms were obtained at 77 K. The Brunauer–Emmett–Teller (BET) surface area was calculated from the linear part of the BET plot. Raman spectroscopy was carried out using a WITEC CRM200 Raman system equipped with a 532 nm laser source and 100× objective lens. The Beneq TFS 200 thin film system was used for ALD.

Electrochemical evaluation

The Swagelok-type batteries were assembled in an Ar-filled glovebox (Mbraun, Unilab, Germany) by directly using the TFAs (0.016 g; $m_{CTs} = 0.0064$ g, $m_{TiO_2} = 0.0056$ g, $m_{Fe_2O_3} = 0.004$ g), TRAs (0.017 g; $m_{CTs} = 0.009$ g, $m_{TiO_2} = 0.008$ g) and pristine CTs (0.005 g) as the anode materials (the conductivity of the CTs is ca. 0.12 Ω^{-1}), a Li-metal circular foil (0.59 mm thick) as the counter and reference electrode, a microporous polypropylene membrane as the separator, and 1 M solution of $LiPF_6$ in ethylene carbonate (EC) and diethyl carbonate (DEC) (1 : 1 by volume) as the electrolyte. The cell was aged for 15 h before measurement. The discharge–charge cycling was performed at room temperature by using a multichannel battery tester (model SCN, USA).

3. Results and discussion

Fig. 1 schematically illustrates the fabrication process of highly ordered TFAs. First, the surface of CTs was coated with TiO_2 nanoparticles using ALD. Fig. S1† shows the typical morphologies of pristine CTs and as-synthesized TiO_2 seed-assisted CTs, revealing the average diameters of pure carbon fibers and TiO_2 nanoparticles are in the range of 7–9 μm and 100 nm, respectively. After the formation of the TiO_2 seeds, the sample was subjected to the hydrothermal growth at 150 °C for 12 h to form
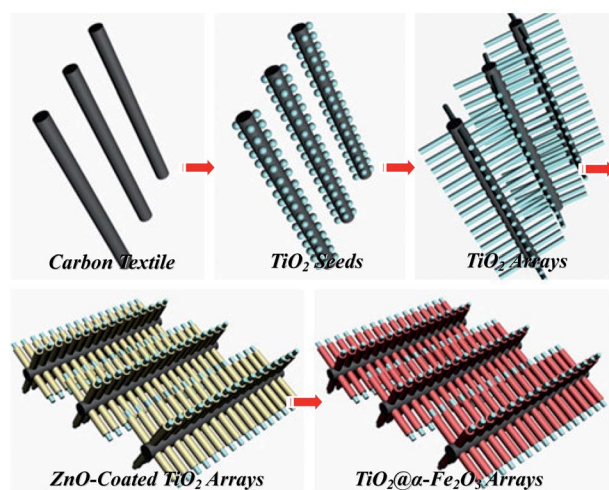
TRAs. The SEM image of as-obtained TRAs shows well-aligned TiO_2 nanorods (Fig. S2a†). The close observation reveals that an individual TiO_2 nanorod is typically with a length of about 3–5 μm and diameter of ∼500 nm in the middle part (Fig. S2b†). The SEM images of the Z-TRAs are presented in Fig. S2c and d†. The nanorods present rough surface with ZnO nanoparticles in the shells. When the Z-TRAs were immersed in an aqueous solution of $Fe(NO_3)_3 \cdot 9H_2O$ at room temperature, a layer of $Fe(OH)_3$ colloid was uniformly and compactly covered on the surface of TiO_2 nanorods. Further annealing enables the formation of TFAs (Fig. 2). Fig. 2a–e show the SEM images of the TFAs at different magnifications, respectively. From the SEM observations, it can be seen that the surface of TFAs contains numerous nanoparticles, the length of an individual TFA ranges from 1 to 3 μm and the diameter of about 600 nm, and almost all of the TFAs show the same morphology. To demonstrate that the whole arrays are converted into TFAs, compositions of the TFAs were characterized by Raman spectroscopy. The existence of the pure phase of TiO_2 and α-Fe_2O_3 is clearly reflected in the Raman spectra (Fig. 2f).[42] The absence of ZnO Raman modes indicates the complete consumption of the ZnO nanoparticles. The TFAs are strongly anchored onto the CTs with good adhesion. The robust mechanical adhesion observed indicates that no material loss occurred after sonication in solution for several minutes, which is very promising for improving electrochemical performance of the electrode. Moreover, the optical image of the TFAs of the formation processes is provided in Fig. 3 and the flexible display is shown in Fig. S3†.
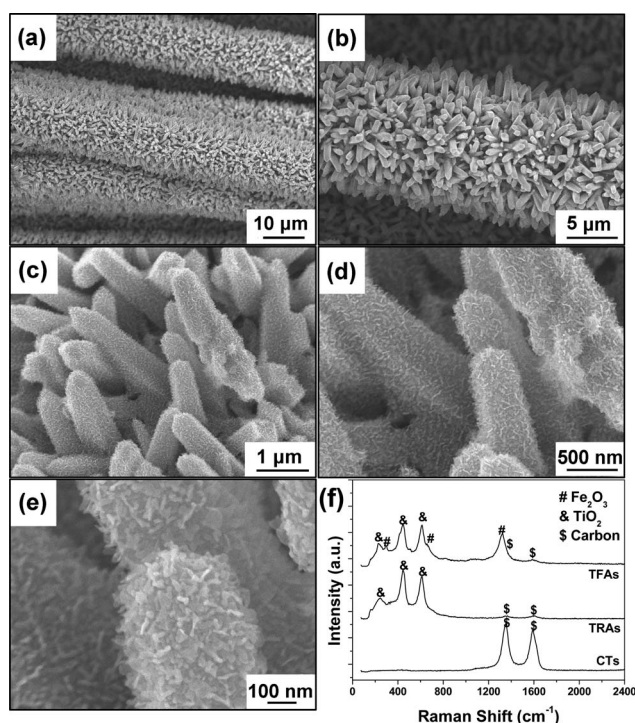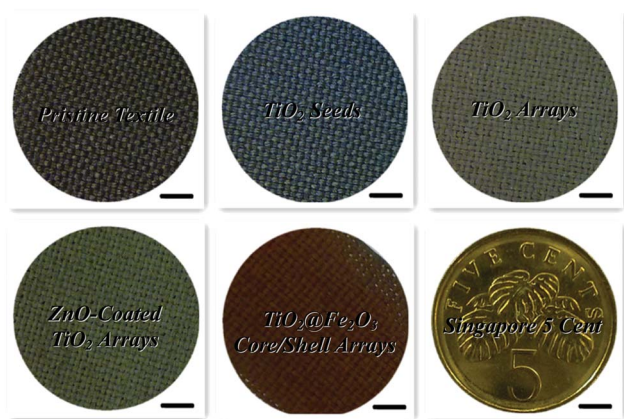

Fig. 1 Schematic illustration of the formation processes of the TFAs.

Fig. 2 (a and b) Low-magnification SEM images of TFAs. (c–e) High-resolution SEM images of TFAs at various magnifications. (f) Raman spectra of TFAs. The spectra of pure CTs and TRAs are also shown for comparison.

This journal is © The Royal Society of Chemistry 2012

Energy Environ. Sci., 2012, **5**, 6559–6566 | 6561

Fig. 3 Optical image of the formation processes of the TFAs. Scale bar: 3 mm.

The structures of the TFAs were further investigated by TEM and HRTEM. Fig. 4a shows a typical TEM image of a TiO_2 nanorod. Examination of an individual nanorod with HRTEM shows that it is completely crystalline along its entire length
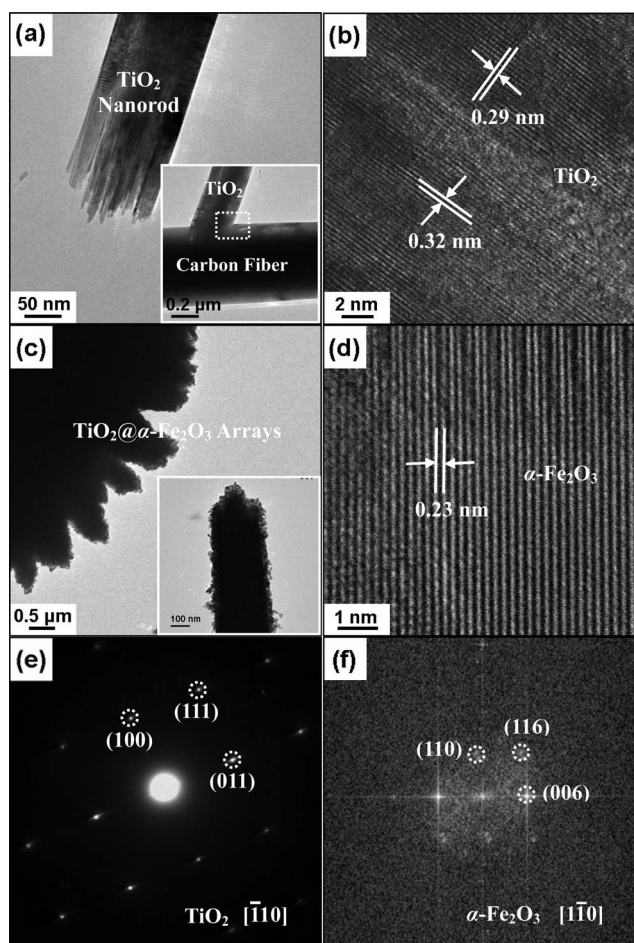
Fig. 4 (a and b) Low-magnification and high-magnification TEM images of a TiO_2 nanorod. (c) Low-magnification TEM image of TFAs. (d) HRTEM image of the α-Fe_2O_3 shell. (e) SAED pattern of a TiO_2 nanorod. (f) Fast Fourier transformation pattern of the HRTEM image of the α-Fe_2O_3 shell in (d).

(Fig. 4b). Lattice fringes with spacings of 0.32 nm and 0.29 nm are attributed to the interplanar spacings of the (110) and (001) planes of rutile TiO_2, respectively. The inset of Fig. 4a displays the interface region of the hybrids, from which a good connection between the TiO_2 branch and the carbon fiber backbone can be clearly seen. The TEM image in Fig. 4c shows a portion of the TFAs hierarchical nanostructure. Across the core/shell structure, we find that the highly dense α-Fe_2O_3 particles are located around the TiO_2 nanorod surface. A typical TEM image of an individual TFA sample is shown in the inset of Fig. 4c, revealing that the TiO_2 nanorod is coated fully with 20–60 nm sized α-Fe_2O_3 particles. The diameter of α-Fe_2O_3 particles is not uniform, which is a characteristic of the solution-grown hierarchical nanostructure. The fringe spacing of 0.23 nm matches well with the interplanar spacing of the (006) planes of the α-Fe_2O_3. The TiO_2 nanorods are single-crystalline, as evidenced by the sharp SAED pattern of a nanorod examined along the $[\bar{1}10]$ zone axis (Fig. 4e). Two-dimensional fast Fourier transform (FFT) of the lattice image of the α-Fe_2O_3 shell is also given, as shown in Fig. 4f, which is consistent with the XRD data (not shown here). The EDS spectrum reveals that the TFAs are composed of the elements of Ti, C, O, and Fe (Fig. S4†). The signal of Cu is from the copper net; the signals of Ti, Fe, and O are attributed to the TFAs, and the C signal results from the CTs. No Zn signal is observed in the EDS, indicating that the as-prepared sample is highly purified TFAs. More details of the nanostructure of the TFAs can be found in Fig. S5†.

Evidence of the composition evolution is given by XRD. Fig. 5 illustrates the XRD patterns of the primary CTs, TRAs, Z-TRAs, and TFAs (labeled as a–d). For curve a, the (002) reflection peak of CTs is very broad and weak owing to a poorly crystallized compound originating from the effect of amorphous carbon. The crystal phase of TRAs is the tetragonal rutile phase (space group: $P4_2/mnm$, $a = b = 0.4517$ nm and $c = 0.2940$ nm). As for the Z-TRAs hybrids, all of the diffraction peaks can be indexed as a mixture of hexagonal wurtzite ZnO (space group: $P6_3/mc$, $a = 0.3249$ nm, $c = 0.5206$ nm) and tetragonal rutile TiO_2, which is consistent with the JCPDS file no. 079-2205 and 88-1175, respectively. After being immersed in Fe^{3+} solution for 24 h and further calcinated in Ar at 450 °C, ZnO peaks
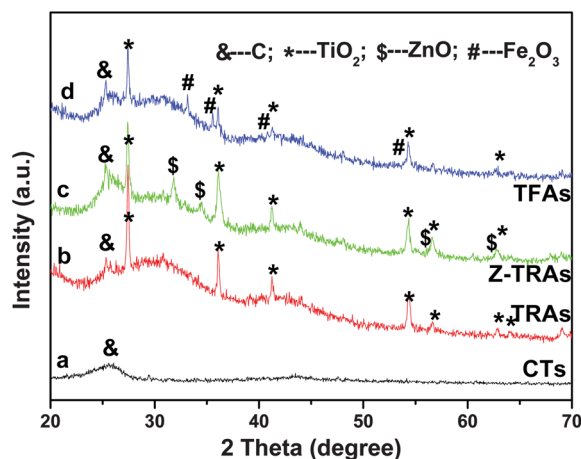
Fig. 5 XRD patterns of the primary CTs (curve a), TRAs (curve b), Z-TRAs (curve c) and TFAs (curve d).

disappeared completely and transformed into the phase of α-Fe_2O_3. The three peaks located at 33.1°, 35.6°, and 54.1° match well with the (104), (110), and (116) planes of α-Fe_2O_3 as evidenced from the XRD pattern (curve d, JCPDS file no. 33-0664), indicating the formation of α-Fe_2O_3 shells. These conclusions were also confirmed by the above-mentioned HRTEM and SAED measurements.

The surface chemical compositions and the valence states of TFAs were revealed by XPS (Fig. 6). To identify all the states of carbon, oxygen, titanium and iron elements, we deconvoluted the C 1s, O 1s, Ti 2p and Fe 2p. Fig. 6a shows the XPS spectrum of the C 1s core-level, which is decomposed into four peaks of 284.8, 286.4, 288, and 290 eV, respectively.[43] These components can be assigned to C from nonoxygenated carbon (CC), COC/COH, a carbonyl group (CO), and a COOH group. This result clearly indicates that a certain degree of oxidation is carried out when obtaining TFAs. The deconvolution peaks (Fig. 6b) of the O 1s spectrum are also resolved into four components, centered at 530, 531.3, 532.7, and 534.8 eV, respectively. The low binding energy component observed at 530 eV is attributed to the O^{2-} forming oxide with titanium and iron elements, the latter three peaks are assigned to OH^-, C–O and O–C=O, and H_2O, respectively.[44–46] Fig. 6c presents the XPS spectra of Ti 2p doublet peaks; the binding energy of Ti $2p_{1/2}$ and Ti $2p_{3/2}$ was observed at approximately 465.7 eV and 459.9 eV, respectively. The splitting data between the Ti $2p_{1/2}$ and Ti $2p_{3/2}$ core levels are 5.8 eV, indicating a normal state of Ti^{4+} in the anatase TiO_2. Similarly, the core level spectra of Fe 2p were curve fitted and are shown in Fig. 6d. There are five multiplet peaks for Fe 2p observed in the spectra. Peaks corresponding to 708.4 eV and

721.6 eV are attributed to 2+ oxidation states, whereas 710.5 eV and 723.4 eV are ascribed to 3+ oxidation states of iron. The peak centered at 715.5 eV is identified as the surface peak of α-Fe_2O_3.[46,47] In addition, the surface area of the TFAs, CTs and TRAs was determined by nitrogen adsorption–desorption measurement at 77 K. The recorded adsorption and desorption isotherms for the TFAs show a significant hysteresis (Fig. S6a†), the BET surface area for the TFAs calculated from the linear part of the BET plot is about 21.9 m^2 g^{-1}, which is larger than that for CTs ($\sim$0 m^2 g^{-1}) and TRAs ($\sim$0 m^2 g^{-1}), respectively (Fig. S6b and c†). This is attributed to the fact that the surfaces of the TFAs contain numerous thorn-shaped nanostructures. Barrett–Joyner–Halenda (BJH) calculations for the pore size distribution, derived from desorption data, reveal a wide distribution for the TFA nanostructures centered at 3 nm (inset of Fig. S6a†). Such nanostructures with much higher surface area have good performances for LIBs.

Discharge–charge measurement for the TFAs was carried out in the potential range of 5 mV to 3.0 V (vs. Li) at a current density of 120 mA g^{-1} up to 150 cycles at ambient temperature (RT), and the voltage versus capacity profiles are shown in Fig. 7a. In the discharge curve of the first cycle there are three obvious voltage plateaus ($\sim$1.75, $\sim$1.2 and $\sim$0.8 V), resulting from the lithium reactions with TiO_2 and Fe_2O_3 nanomaterials. The first plateau at $\sim$1.75 V is associated with the phase transition between the tetragonal TiO_2 and orthorhombic Li_xTiO_2 phases.[48–50] The second plateau at $\sim$1.2 V can be ascribed to the formation of cubic $Li_2Fe_2O_3$,[51] and the third plateau at $\sim$0.8 V reflects the reduction from Fe^{2+} to Fe^0 and the formation of amorphous Li_2O.[28,52] The charge curve shows a broad sloping plateau
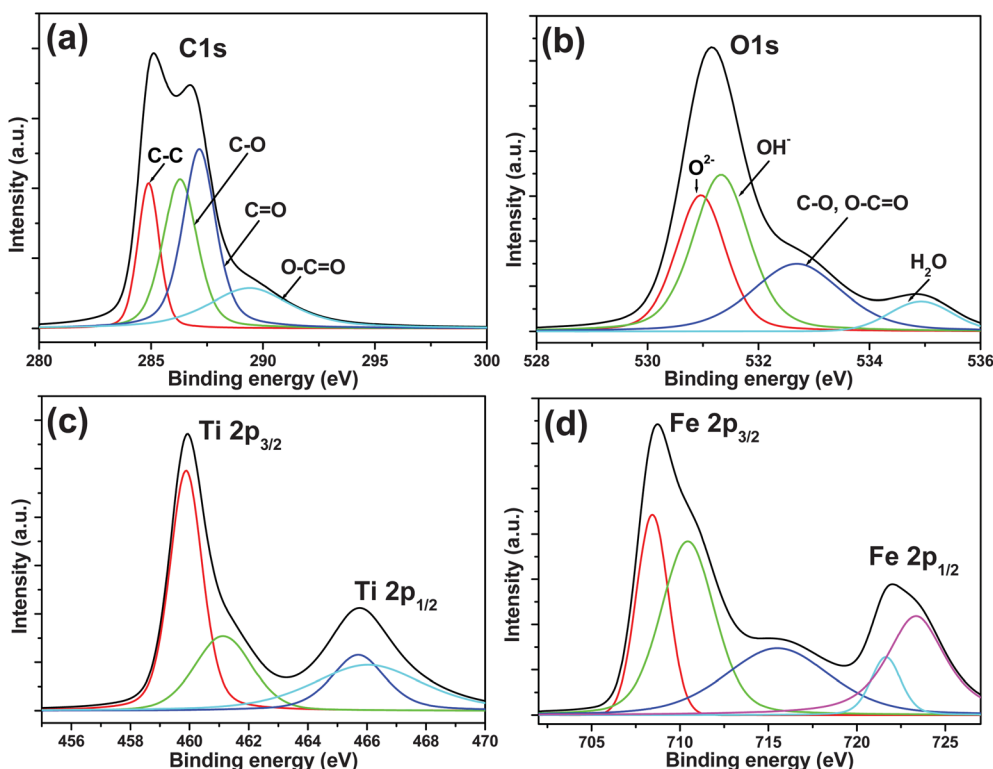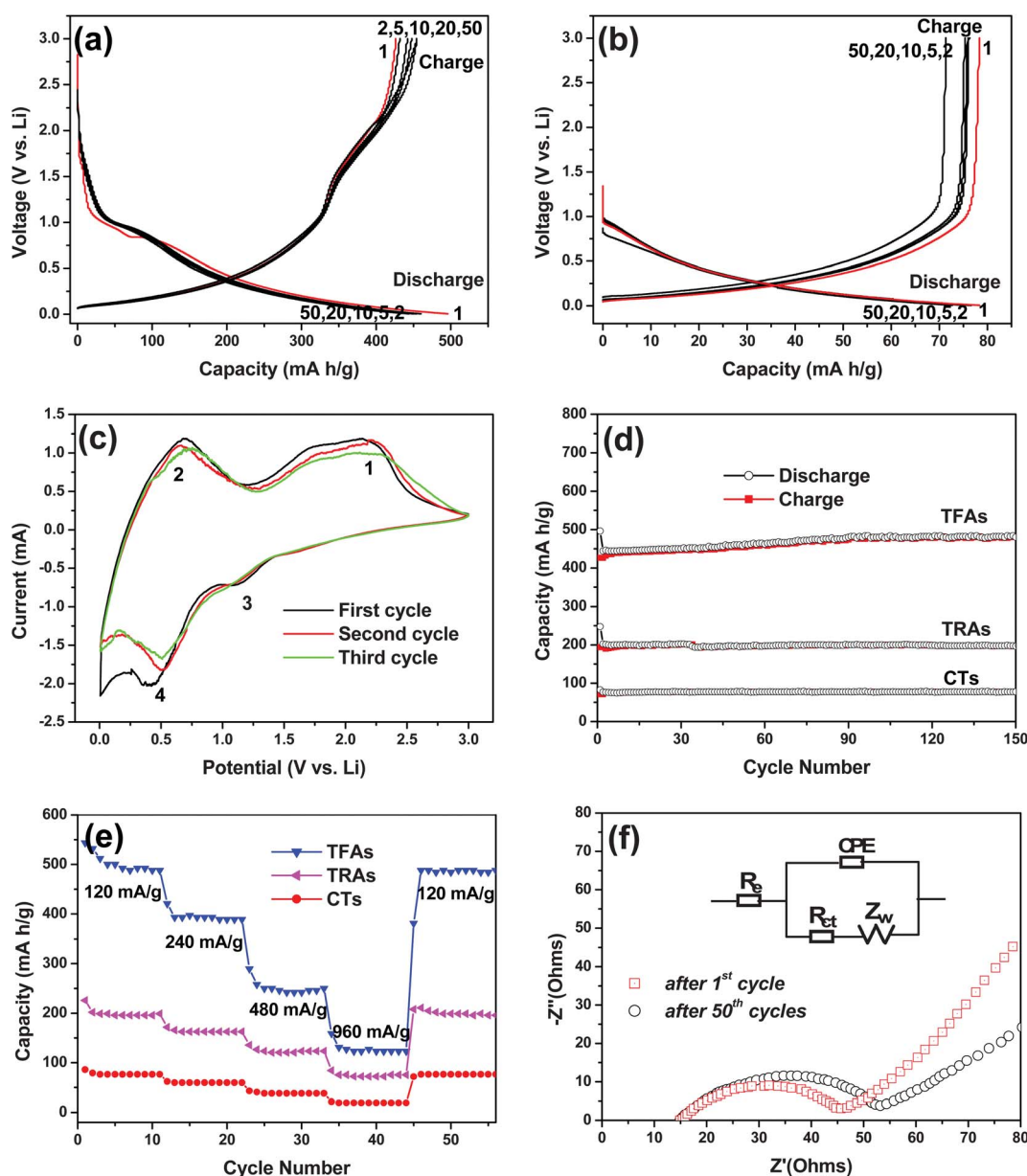

Fig. 6 XPS spectra of (a) C 1s, (b) O 1s, (c) Ti 2p and (d) Fe 2p regions of the TFAs.

Fig. 7 Galvanostatic discharge/charge profiles of the TFAs anode (a) and the CTs anode (b) at a constant current density of 120 mA g⁻¹. (c) CV curve of a TFAs anode at 0.5 mV s⁻¹ scanning rate. (d) Cycling performance of the anodes at a constant current density of 120 mA g⁻¹. (e) Reversible capacity *vs.* current density (rate capability) for different anodes. (f) Equivalent circuit and electrochemical impedance spectra after the 1st and 50th cycles.

(1.4–2.1 V) due to the reversible reactions. It can be seen that the first discharge and charge capacities are ~497 and ~422 mA h g⁻¹, respectively. The voltage–capacity trace of CTs was also recorded for comparison (Fig. 7b). Moreover, one can see a negligible irreversible capacity loss from the first two cycles. The discharge–charge profiles also indicate that the curves overlap reasonably well during the 5–50 cycles, as shown in Fig. 7a. This result suggests that full and stable capacity is realized owing to the special structure of the TFAs.

Cyclic voltammetry (CV) was carried out to understand the reactive process. Li metal was used as the counter and reference electrodes. Fig. 7c shows the first three CV curves of TFAs at room temperature in the range of 0.005–3.0 V at a slow scan rate of 0.5 mV s⁻¹. As can be seen, the cathodic peaks (first sweep)

located around ~0.6 V with a shoulder at about ~1.2 V can be attributed to the formation of Li₂O as well as the SEI film. The subsequent well-defined anodic peaks are observed at ~0.7 V and ~2.1 V, indicating the extraction of Li⁺ in the electrode materials. These results nearly coincide with the voltage plateaus in the galvanostatic discharge–charge curve (Fig. 7a). The second cathodic sweep differs slightly from the first one, indicating different redox behaviour. It is worth noting that the CV peaks overlap well during the subsequent cycles. This means that the electrochemical reaction becomes highly reversible after the first discharge–charge, which is consistent with its good cycling performance as discussed below. Moreover, cyclic voltammograms were also investigated on the cells with CTs and TRAs for comparison (Fig. S7†).

The capacity *versus* cycle number plot is shown in Fig. 7d. As can be seen, it is evident that the TFAs electrode exhibits exceptional cyclability. Although the capacity increases gradually in the first 90 cycles, it stabilizes at around $\sim$480 mA h g^{-1} in the following 60 cycles. The capacity enhancement can be mainly attributed to one reason that along the increase of cycle numbers, more reacting sites of TFAs have been activated, participating in the lithium-ion storage and making contribution to the final capacity. In order to clarify the influence of the hybridization on the electrochemical performance of the TFAs, we have calculated the theoretical capacity of the physical mixture of pristine materials (CTs, TiO$_2$ and Fe$_2$O$_3$) from the theoretical capacities of the CTs (372 mA h g^{-1}), TiO$_2$ (335 mA h g^{-1}) and Fe$_2$O$_3$ (1005 mA h g^{-1}), respectively. The chemical compositions of TFAs are calculated with 40% of CTs, 35% of TiO$_2$ and 25% of Fe$_2$O$_3$. On the basis of the equation described below, we could calculate a theoretical capacity (C) of the TFAs,[53] as follows: $C_{\text{theoretical}} = C_{\text{CTs}} \times \%_{\text{mass of CTs}} + C_{\text{TiO}_2} \times \%_{\text{mass of TiO}_2} + C_{\text{Fe}_2\text{O}_3} \times \%_{\text{mass of Fe}_2\text{O}_3} = 372 \times 0.4 + 335 \times 0.35 + 1005 \times 0.25 = 517.3$ mA h g^{-1}. The results show that the TFAs can deliver a high discharge capacity of 480 mA h g^{-1} that is equal to 93% of the theoretical capacity. Of course, this theoretical capacity is an approximate value owing to the existence of additional lithium storage sites in our TFAs.[54,55] The capacity–voltage profiles of the TRAs and CTs also show relatively steady and no noticeable capacity fading. Whereas, only capacities of $\sim$80 and $\sim$200 mA h g^{-1} can be observed at the process of 150 cycles, respectively. In core/shell systems, for instance, there are still some obstacles. Yamada *et al.* and many other researchers have tried to improve the performance of V$_2$O$_5$ by designing core/shell structures to achieve better rate capability,[56,57] the result is still unsatisfactory owing to suffering from low cycling stability. The core/shell Si@C composites including Si nanoparticles and 1D nanomaterials showed greatly enhanced specific capacities and high-rate stability,[58,59] they are still far from practical utilization due to their complicated preparation route, high cost, and low tap density. As a result, our strategy presented may prove to be cost-effective, scalable, and environmentally friendly. Hence, the special structure of TFAs with good adhesion of the core/shell and the current collector, and maintenance of integrity structure during Li insertion/extraction cycles, plays an important role in giving rise to the remarkable stability as well as good capacity retention. For a better understanding of the rate performance of the TFAs in lithium energy storage, the cycling response at continuously variable rates was evaluated (Fig. 7e). All of the electrodes were first cycled at a current density of 120 mA g^{-1}. Irreversible capacity losses during the initial two cycles are observed for the electrodes presumably due to decomposition of the electrolyte and/or solvent. Nevertheless, the first discharge capacity of $\sim$480 mA h g^{-1} for the TFAs is higher than those of the TRAs ($\sim$198 mA h g^{-1}) and the CTs ($\sim$76 mA h g^{-1}). Subsequently, the current density is increased stepwise to 240 mA g^{-1}, the specific capacity of the TFAs is $\sim$392 mA h g^{-1}, which is slowly reduced to $\sim$242 mA h g^{-1} at 480 mA g^{-1} and $\sim$121 mA h g^{-1} at 960 mA g^{-1}, respectively. After 50 cycles, with the current rate being again decreased back to 120 mA g^{-1}, a capacity of $\sim$479 mA h g^{-1} can be recovered. These capacities are also higher than those of the electrode made of TRAs and CTs under the same conditions. The excellent rate performance and cyclability render the TFAs very promising candidate for LIBs application.

To gain further insight into the electrochemical performances, electrochemical impedance spectroscopy (EIS) measurements were carried out at room temperature on cells after the 1st and 50th cycles (Fig. 7f). The EIS data are analyzed by fitting to an equivalent electrical circuit shown in the inset of Fig. 7f, similar to the circuit employed for other oxide electrodes.[28,60,61] The result shows that the Nyquist plot exhibits two distinct parts including a semicircle in the high frequency region and a sloped line in the low frequency region, further demonstrating the long-term electrochemical stability of these electrode materials. The TFAs after the 1st and 50th cycles show the charge transfer resistances (R_{ct}) of 32.3 and 40.4 Ω, respectively. The R_{ct} value increases only slightly from the 1st to the 50th cycle owing to the good contact among the core/shell arrays as well as between the current-collector and core/shell arrays. Nevertheless, many factors may contribute to the superior performance of our novel hybrid nanocomposite. Among them, the highly ordered core/shell arrays on carbon substrates are undoubtedly the key to the capacity retention on cycling, especially at high discharge–charge rates.

4. Conclusions

We have combined the stepwise, seed-assisted hydrothermal approach to design the highly ordered TFAs as the anode materials for Li-ion batteries. The TFAs exhibit $\sim$497 and $\sim$422 mA h g^{-1} for the first discharge and charge capacities at a current density of 120 mA g^{-1}, respectively. It shows good capacity retention with $\sim$480 mA h g^{-1} after the 150th discharge–charge cycle, as well as high rate capability. The total specific capacity of the TFAs is higher than the sum of TRAs and CTs, indicating a synergistic effect between the constituents of the composite structure on the electrochemical performance. The dramatic improvement in the LIB performance can be ascribed to the advantages endowed by the well-ordered active nanostructure arrays grown directly on carbonaceous matrices, such as good contact of the active materials and adhesion with the current collector, large interfacial area for lithium insertion/extraction, and reduced ion diffusion pathways. The synthetic strategy of such nanoarchitecture electrode could be extended to other active oxides, thus creating new opportunities for designing a wide range of high-performance LIB electrode materials.

Acknowledgements

Notes and references

1 M. Armand and J. M. Tarascon, *Nature*, 2008, **451**, 652.
2 M. R. Palacin, *Chem. Soc. Rev.*, 2009, **38**, 2565.
3 P. Poizot and F. Dolhem, *Energy Environ. Sci.*, 2011, **4**, 2003.
4 L. W. Ji, Z. Lin, M. Alcoutlabi and X. W. Zhang, *Energy Environ. Sci.*, 2011, **4**, 2682.

5 X. J. Zhu, Y. W. Zhu, S. Murali, M. D. Stoller and R. S. Ruoff, *ACS Nano*, 2011, **5**, 3333.
6 W. W. Zhou, J. X. Zhu, C. W. Cheng, J. P. Liu, H. P. Yang, C. X. Cong, C. Guan, X. T. Jia, H. J. Fan, Q. Y. Yan, C. M. Li and T. Yu, *Energy Environ. Sci.*, 2011, **4**, 4954.
7 Z. J. Fan, J. Yan, T. Wei, G. Q. Ning, L. J. Zhi, J. C. Liu, D. X. Cao, G. L. Wang and F. Wei, *ACS Nano*, 2011, **5**, 2787.
8 Z. L. Gong and Y. Yang, *Energy Environ. Sci.*, 2011, **4**, 3223.
9 L. Lu, H. yang and J. Burnett, *Renewable Energy*, 2002, **27**, 1.
10 C. Uhuegbu, *J. Emerging Trends Eng. Appl. Sci.*, 2011, **2**, 96.
11 C. X. Guo, M. Wang, T. Chen, X. W. Lou and C. M. Li, *Adv. Energy Mater.*, 2011, **1**, 736.
12 Y. L. Liang, R. J. Feng, S. Q. Yang, H. Ma, J. Liang and J. Chen, *Adv. Mater.*, 2011, **23**, 640.
13 S. B. Yang, H. H. Song and X. H. Chen, *Electrochem. Commun.*, 2006, **8**, 137.
14 L. Zhao, Y. S. Hu, H. Li, Z. X. Wang and L. Q. Chen, *Adv. Mater.*, 2011, **23**, 1385.
15 S. B. Yang, X. L. Feng and K. Müllen, *Adv. Mater.*, 2011, **23**, 3575.
16 R. A. Huggins, *Solid State Ionics*, 1998, **57**, 113.
17 C. M. Park and H. J. Sohn, *Adv. Mater.*, 2010, **22**, 47.
18 R. Teki, M. K. Datta, P. Krishnan, T. C. Parker, T. M. Lu, P. N. Kumta and N. Koratkar, *Small*, 2009, **5**, 2236.
19 A. D. W. Todd, P. P. Ferguson, M. D. Fleischauer and J. R. Dahn, *Int. J. Energy Res.*, 2010, **34**, 535.
20 J. Cabana, L. Monconduit, D. Larcher and M. R. Palacin, *Adv. Mater.*, 2010, **22**, E170.
21 E. Kang, Y. S. Jung, A. S. Cavanagh, G. H. Kim, S. M. George, A. C. Dillon, J. K. Kim and J. Lee, *Adv. Funct. Mater.*, 2011, **21**, 2430.
22 J. Li, H. M. Dahn, L. J. Krause, D. B. Le and J. R. Dahn, *J. Electrochem. Soc.*, 2008, **155**, A812.
23 Y. S. Jung, S. Lee, D. Ahn, A. C. Dillon and S. H. Lee, *J. Power Sources*, 2009, **188**, 286.
24 A. C. Siegel, S. T. Phillips, M. D. Dickey, N. Lu, Z. Suo and G. M. Whitesides, *Adv. Funct. Mater.*, 2010, **20**, 28.
25 A. W. Martinez, S. T. Phillips, M. J. Butte and G. M. Whitesides, *Angew. Chem., Int. Ed.*, 2007, **46**, 1318.
26 A. S. Aricò, P. Bruce, B. Scrosati, J. M. Tarascon and W. V. Schalkwijk, *Nat. Mater.*, 2005, **4**, 366.
27 V. Etacheri, R. Marom, R. Elazari, G. Salitra and D. Aurbach, *Energy Environ. Sci.*, 2011, **4**, 3243.
28 M. V. Reddy, T. Yu, C. H. Sow, Z. X. Shen, C. T. Lim, G. V. S. Rao and B. V. R. Chowdari, *Adv. Funct. Mater.*, 2007, **17**, 2792.
29 J. H. Liu, J. S. Chen, X. F. Wei, X. W. Lou and X. W. Liu, *Adv. Mater.*, 2011, **23**, 998.
30 M. M. Rahman, J. Z. Wang, M. F. Hassan, D. Wexler and H. K. Liu, *Adv. Energy Mater.*, 2011, **1**, 212.
31 Y. S. Hu, L. Kienle, Y. G. Guo and J. Maier, *Adv. Mater.*, 2006, **18**, 1421.
32 Y. G. Guo, Y. S. Hu, W. Sigle and J. Maier, *Adv. Mater.*, 2007, **19**, 2087.
33 L. B. Hu, H. Wu, F. L. Mantia, Y. Yang and Y. Cui, *ACS Nano*, 2010, **4**, 5843.

34 X. Xie, M. Pasta, L. B. Hu, Y. Yang, J. McDonough, J. Cha, C. S. Criddle and Y. Cui, *Energy Environ. Sci.*, 2011, **4**, 1293.
35 K. Jost, C. R. Perez, J. K. McDonough, V. Presser, M. Heon, G. Dion and Y. Gogotsi, *Energy Environ. Sci.*, 2011, **4**, 5060.
36 D. Deng and J. Y. Lee, *Angew. Chem., Int. Ed.*, 2009, **48**, 1660.
37 Y. Qiu, K. Yan and S. Yang, *Chem. Commun.*, 2010, **46**, 8359.
38 Y. Yu, L. Gu, C. Wang, A. Dhanabalan, P. A. van Aken and J. Maier, *Angew. Chem., Int. Ed.*, 2009, **48**, 6485.
39 J. P. Liu, Y. Y. Li, X. T. Huang, R. M. Ding, Y. Y. Hu, J. Jiang and L. Liao, *J. Mater. Chem.*, 2009, **19**, 1859.
40 B. Liu and E. S. Aydil, *J. Am. Chem. Soc.*, 2009, **131**, 3985.
41 L. E. Greene, M. Law, D. H. Tan, M. Montano, J. Goldberger, G. Somorjai and P. D. Yang, *Nano Lett.*, 2005, **5**, 1231.
42 T. Yu, Y. Zhu, X. Xu, K. S. Yeong, Z. Shen, P. Chen, C. T. Lim, J. T. L. Thong and C. H. Sow, *Small*, 2006, **2**, 80.
43 L. Tang, Y. Wang, Y. Li, H. Feng, J. Lu and J. Li, *Adv. Funct. Mater.*, 2009, **19**, 2782.
44 G. Bhargava, I. Gouzman, C. M. Chun, T. A. Ramanarayanan and S. L. Bernasek, *Appl. Surf. Sci.*, 2007, **253**, 4322.
45 T. Yamashita and P. Hayes, *Appl. Surf. Sci.*, 2008, **254**, 2441.
46 G. K. Pradhan and K. M. Parida, *ACS Appl. Mater. Interfaces*, 2011, **3**, 317.
47 A. P. Grosvenor, B. A. Kobe, M. C. Biesinger and N. S. McIntyre, *Surf. Interface Anal.*, 2004, **36**, 1564.
48 M. A. Reddy, M. S. Kishore, V. Pralong, V. Caignaert, U. V. Varadaraju and B. Raveau, *Electrochem. Commun.*, 2006, **8**, 1299.
49 G. Sudant, E. Baudrin, D. Larcher and J. M. Tarascon, *J. Mater. Chem.*, 2005, **15**, 1263.
50 C. H. Jiang, M. D. Wei, Z. M. Qi, T. Kudo, I. Honma and H. S. Zhou, *J. Power Sources*, 2007, **166**, 239.
51 J. Morales, L. Sanchez, F. Martin, F. Berry and X. L. Ren, *J. Electrochem. Soc.*, 2005, **152**, A1748.
52 X. L. Wu, Y. G. Guo, L. J. Wan and C. W. Hu, *J. Phys. Chem. C*, 2008, **112**, 16824.
53 S. M. Paek, E. J. Yoo and I. Honma, *Nano Lett.*, 2009, **9**, 72.
54 W. B. Yue, C. Randorn, P. S. Attidekou, Z. X. Su, J. T. S. Irvine and W. Z. Zhou, *Adv. Funct. Mater.*, 2009, **19**, 2826.
55 S. W. Kim, T. H. Han, J. Kim, H. Gwon, H. S. Moon, S. W. Kang, S. O. Kim and K. Kang, *ACS Nano*, 2009, **3**, 1085.
56 H. Yamada, K. Tagawa, M. Komatsu, I. Moriguchi and T. Kudo, *J. Phys. Chem. C*, 2007, **111**, 8397.
57 K. Takahashi, Y. Wang and G. Z. Cao, *J. Phys. Chem. B*, 2005, **109**, 48.
58 B. Hertzberg, A. Alexeev and G. Yushin, *J. Am. Chem. Soc.*, 2010, **132**, 8548.
59 L. F. Cui, R. Ruffo, C. K. Chan, H. Peng and Y. Cui, *Nano Lett.*, 2009, **9**, 491.
60 G. X. Wang, L. Yang, Y. Chen, J. Z. Wang, S. Bewlay and H. K. Liu, *Electrochim. Acta*, 2006, **51**, 4634.
61 H. C. Shin, W. I. Cho and H. Jang, *J. Power Sources*, 2006, **159**, 1383.